International Journal of Thermal Sciences 162 (2021) 106786

Contents lists available at ScienceDirect

International Journal of Thermal Sciences

journal homepage: http://www.elsevier.com/locate/ijts

Modeling the lightning continuing current electric arc discharge and material thermal damage: Effects of combinations of amplitude and duration

Yakun Liu [a,b], Yeqing Wang [c,*]

[a] Department of Electrical Engineering, Shanghai Jiao Tong University, Shanghai, 20030, China
[b] Department of Civil and Environmental Engineering, Massachusetts Institute of Technology, Cambridge, MA, 02139, USA
[c] Department of Mechanical and Aerospace Engineering, Syracuse University, Syracuse, NY, 13244, USA

ARTICLE INFO

Keywords:
Lightning strike
Electric arc plasma
Material thermal damage
Heat flux
Multiphysics model
Finite element analysis

ABSTRACT

The damage depth of a material is a key parameter for industrial objects in consideration of the lightning threat. The continuing current component in a multiple lightning sequence features a large charge transfer, which often leads to the dominant damage depth for electrically conductive materials. Laboratory simulation of the lightning continuing current is prone to misinterpretation due to various combinations of the current amplitude and duration in fulfillment of the fixed charge requirement of 200 C (±20%) in standards. This study employs a Unified Plasma-Material Finite Element Model (UPM-FEM) that is developed based on the classical magneto-hydrodynamics method to analyze the influence of the current amplitude-duration combinations on the arc-material interactions. The energy originated from different physical processes, the heat flux and current density on material surface, and the material damage response are predicted using the UPM-FEM and compared for different amplitude-duration combinations at a fixed transfer charge. We report that the Joule heating, thermal conduction, radiative emission, and electronic enthalpic flux jointly determine the energy budget injected to materials at low current levels (≤300 A). While at higher currents (≥500 A), the thermal conduction contributes less significantly compared to the other energy items. The more pronounced increase of radiative emission heat loss will bring a saturation trend in arc properties and the material damage. A combination with a big current amplitude is recommended for achieving consistent arc properties and material damage in lightning continuing current test.

1. Introduction

Large floating oil tanks, aircraft, wind turbines, cable bridges, and other important industrial objects or infrastructures encounter lightning strikes inevitably during operation [1,2]. These structures are primarily made of metallic materials and carbon/glass fiber reinforced polymer matrix composite materials. For metallic materials, the direct lightning damage effects mainly manifest as melting, burning, eroding, and blasting [3–6]. For polymeric composites, the direct damage effects are often more complex, which include resin decomposition, delamination, matrix cracking, fiber breakage, fiber vaporization, and dielectric breakdown puncture [7–22]. The information on damage results is of significant importance to evaluate the lightning threat and develop effective protection measures [23]. When excluding the effects of structure extremities (*e.g.,* sharp tip of a wind turbine blade [24,25]), the structures made by electrically conductive materials are more prone to be struck by lightning strikes. This is because the electrons within the metal lattice have a much stronger delocalized mobility and can easily accumulate on the material surface in response to the charged cloud aloft [26].

The damage depth of a material is one of the most concerned parameters for industrial objects in response to the lightning arc [11,14,27–29]. As natural lightning has a big uncertainty on the attachment location, a practical implementation of the lightning certification for material safety is mainly assisted by means of the simulated lightning technology in laboratory to date [27,28,30–32]. The commonly adopted test setup in laboratory is to use an electrode-air-material configuration with a moderate discharge distance [32]. For metallic materials that are

* Corresponding author.
E-mail address: ywang261@syr.edu (Y. Wang).

https://doi.org/10.1016/j.ijthermalsci.2020.106786
Received 28 July 2020; Received in revised form 26 October 2020; Accepted 30 November 2020

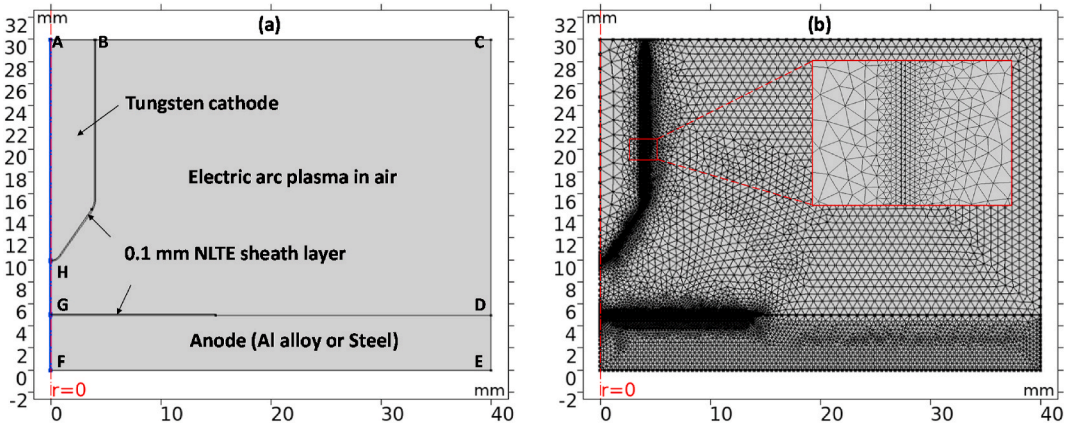

Fig. 1. (a) Problem setup in COMSOL and (b) mesh used in the model.

electrically conductive, the direct heat flux injection on the material surface is the main damage source, as the Joule heating inside materials can be often negligible. Experimental investigations show that the damage depth of metallic materials suffered from lightning is dominated by the charge transfer during the discharge [33]. The continuing current component in a multiple lightning sequence, generally represented by a unidirectional rectangular waveform with an adjustable amplitude of 200–800 A and duration of 0.25–1.0 s, has the largest charge transfer (200 C, ±20%) and is responsible for the most serious damage depth for metallic materials [27,28,34]. At the same time, there exist many possible combinations of current amplitude and duration to fulfill the charge requirement. In arc discharges, the current amplitude has a big impact on the arc temperature and the associated heat flux, arc pressure, and other arc properties. The current duration controls the arc dwell time and the accumulated damage effects. Therefore, the resultant material damage is jointly affected by both the current amplitude and the duration. To date, the influence of current amplitude-duration combinations on arc properties has not been clearly addressed, which is of great significance to improve lightning damage certification tests. It is worth noting that this paper focuses on metallic materials, whose lightning damage behaviors are much simpler than polymeric composite materials. This allows us to extract the fundamental principles governing the lightning energy dissipation in the material more easily and practically. The understanding we acquired on the lightning strike damage of the metallic materials can also provide insights into the lightning damage of polymeric composites.

In this work, a Unified Plasma-Material Finite Element Model (UPM-FEM) is employed to study the influence of current amplitude-duration combinations at a fixed charge transfer on the electric arc characteristics and metal damage caused by the lightning continuing current. The different energy contributions, electric arc characteristics (*e.g.,* distributions of heat flux, current density, and plasma temperature), and material damage results are obtained and discussed in detail. The UPM-FEM is developed using the classical and well-validated magnetohydrodynamics (MHD) method, which is widely used for modeling electric arcs for welding and simulated lightning strike applications [35–42]. Therefore, the novelty of this study is not in the model itself, but rather, it is in using the MHD approach to unravel the effect of different combinations of amplitude and duration at a fixed charge transfer on the competing energy contributions of the electric arc and the resulting material damage. This has never been explored in the past to authors' knowledge. The understanding gained from this study can provide guidance in the design of improved lightning continuing current tests to produce consistent lightning arc energy and consistent material damage, thereby leading to conservative lightning strike protection designs for industrial materials and structures.

The remainder of the paper is organized as follows: a brief introduction of the UPM-FEM and its numerical implementation is presented in Section 2. Section 3 presents the influence of current amplitude-duration combinations at a fixed charge transfer on four competing energy items in the electric arc heating process. The changes in heat flux flowing from the electric arc into the test material surface and the damage response are discussed in Section 4. Conclusions are drawn in Section 5.

2. UPM-FEM and numerical implementation

2.1. UPM-FEM

The Unified Plasma-Material Finite Element Model (UPM-FEM) is developed to study the electric arc characteristics and the damage response of metal materials for simulated lightning continuing current. The test material is set as the cathode or anode in dependence on the polarity of the lightning current. The plasma in the arc column is assumed to be in the local thermodynamic equilibrium (LTE) condition, while the cathode or anode boundary (or sheath) layer is in the non-LTE (NLTE) condition [36,38,41,43]. In the plasma domain, the governing equations solved using FEA include electric current conservation equations, magnetic field equation, heat transfer equation, and Navier-Stokes equations for the MHD. In the cathode and anode domains, the governing equations solved using FEA include electric current conservation equations and the heat transfer energy equations. Note that the NLTE discontinuity along the anode and cathode boundaries is modeled as an ohmic conductor, which ensures the transition between plasma and the electrodes. Within this sheath layer, the electrical conductivity corresponds to the electrodes (*i.e.,* cathode or anode), while the other material properties correspond to the plasma. The same approach of modeling the NLTE discontinuity is used by Ref. [42].

2.2. Numerical implementation

The FEA was implemented with the commercial software COMSOL Multiphysics 5.4. The particular physics modules used in COMSOL include: Heat Transfer, Electric Current, Laminar Flow, Magnetic Fields, and Multiphysics. Here, the Heat Transfer, Electric Current, and Magnetic Fields modules are used to solve the heat transfer equation, electric current conservation equations, and magnetic field equations respectively, in both the plasma domain and the electrode domains (*i.e.,* cathode and anode). The Laminar Flow module is used to solve the Navier-Stokes equations only in the plasma domain. The Multiphysics module is used to achieve data exchange between the different physics modules. The three computational domains, *i.e.,* cathode, plasma, and anode, are shown in Fig. 1 (a).

Geometry - The UPM-FEM created in COMSOL is two-dimensional

Table 1
A summary of the boundary conditions used in the UPM-FEM.

	AB	BC & CD	DE	EF	DG	BH	AF
T	300 K	300 K	300 K	300 K	Ra	Ra	$\frac{\partial T}{\partial r}=0$
u	–	Open BC	0	0	0	0	$\frac{\partial \mathbf{u}}{\partial r}=0$
J	$\mathbf{J}\cdot\mathbf{n}=-J_{in}$	$\mathbf{n}\cdot\mathbf{J}=0$	–	–	–	–	$\frac{\partial \mathbf{J}}{\partial r}=0$
V	–	–	0	0	–	–	$\frac{\partial V}{\partial r}=0$
A	$\mathbf{n}\cdot\mathbf{A}=0$	$\mathbf{n}\cdot\mathbf{A}=0$	$\mathbf{n}\cdot\mathbf{A}=0$	$\mathbf{n}\cdot\mathbf{A}=0$	–	–	$\frac{\partial \mathbf{A}}{\partial r}=0$

and axisymmetric (see Fig. 1(a)). Such a problem setup has been widely used in many existing papers on the modeling of electric arc plasma [35,38,41–43]. The overall computational domain is 40 mm by 30 mm. The cathode has a blunt conical shape, which represents the actual shape of a direct electrode used in many simulated lightning strike tests. Here, it should be mentioned that both direct electrode and indirect electrode configurations are widely used in existing simulated lightning strike tests [32]. The indirect electrode configuration has an insulation cap installed on the electrode head to suppress the electrode jet effect in lightning test. However, this configuration requires using a conductive ignition wire to initiate the arc, which would lead to contamination of the electric arc due to the vaporization of the wire [37]. In contrast, the direct electrode configuration does not require using the ignition wire, and thus, is free from the arc contamination. However, it suffers from the electrode jet effect especially at high electric current. Here, the radius and length of the cathode (*i.e.,* direct electrode) are 4 mm and 10 mm, respectively, the conical angle at the cathode tip is 35°. The arc gap between the cathode and the anode is set to 5 mm. It is worth noting that such an arc gap is chosen to be the same with that used in the first author's prior experimental test setup [3,33,44]. The detailed effect of the arc gap on the arc properties (current density and heat flux) can be found in the literature [45] and is not discussed in this paper. Furthermore, the anode has a thickness of 5 mm. The NLTE layers along the cathode and anode boundaries have a uniform thickness of 0.1 mm [41,42].

Material properties – The material properties of the tungsten cathode and copper anode used in the model are temperature-dependent and taken directly from the COMSOL material library. The plasma domain was assigned with the temperature-dependent transport properties of the air plasma calculated by Boulos et al. and Capitelli et al. [46,47]. It should be mentioned that the zero electrical conductivity of the air at room temperature could lead to numerical divergence. To resolve this issue, we have calculated the initial electrical conductivity of the air using a separate 1-D model (also with COMSOL), which was developed to couple the electron transport and electric current governing equations. The electrical conductivity of the air plasma is initially 1e-14 S/m at room temperature [42]. The model indicates that the electric field quickly rises to 45,000 Townsend at 0.5 μs at the cathode surface, which triggers the electron cold-field emissions and ionization, and hence increases the electrical conductivity of the air plasma. The same approach for resolving the zero electrical conductivity issue is reported in Ref. [42].

Initial and boundary conditions – All computational domains are initially at room temperature. A constant and uniform current density, J_{in} (see Table 1), is converted from the constant current with amplitudes varying from 100 A to 800 A and applied at the top surface of the cathode (see boundary "AB" in Fig. 1(a)). Note that, in this study, we focused on the lightning continuing current, which is one of the lightning components in a multiple lightning sequence. Such a choice is because the duration of the lightning component plays the most important role in determining the material vaporization damage for metallic materials [3,5,33]. Additionally, since the model is axisymmetric, an axial symmetry boundary condition is applied in all physics modules. A summary of the other essential boundary conditions used in the model is listed in Table 1, where "Ra" denotes the surface radiation, T is temperature, u is velocity, J is current density, V is electric potential, and A is magnetic potential.

Meshing – User-controlled mesh was used in COMSOL. Different computational domains were assigned with different mesh densities (see

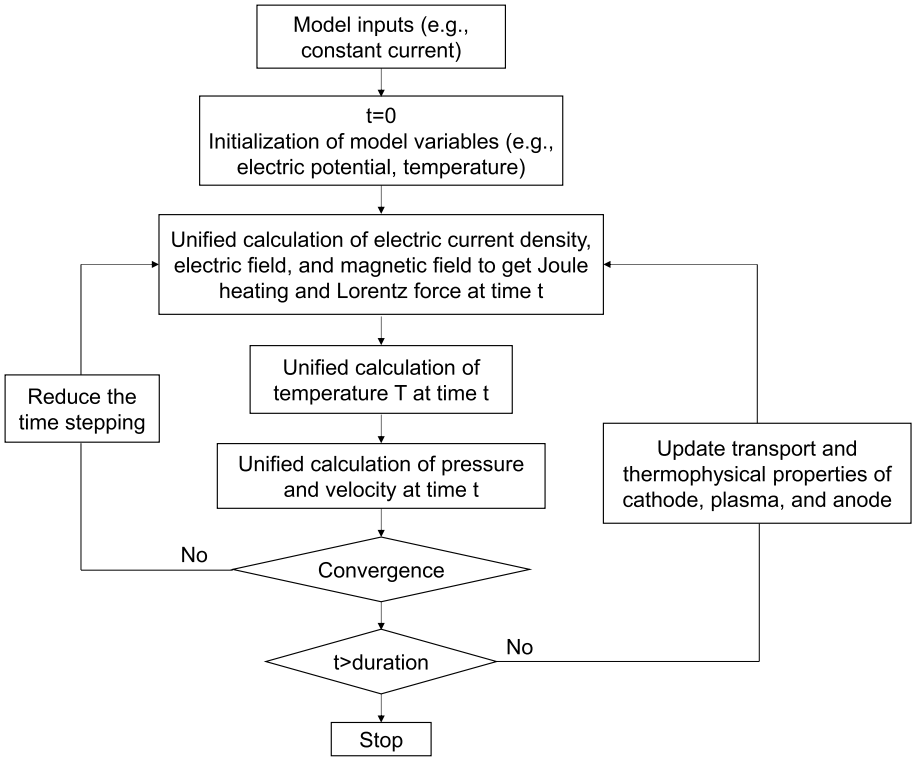

Fig. 2. Flowchart of the calculations of the developed UPM-FEM in COMOSL.

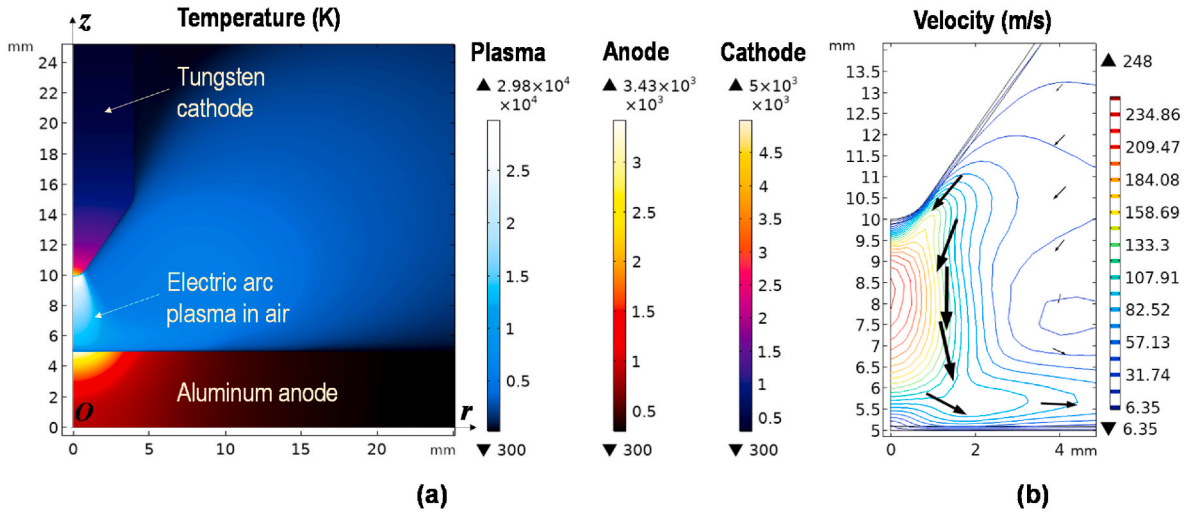

Fig. 3. (a) Temperature distributions within the cathode-plasma-anode domain and (b) the flow velocity of the electric arc plasma at $t = 0.52$ s for a lightning strike continuing current of 404 A.

Table 2
Comparison of model predictions with experimental test data.

	Damaged Depth (mm)		Rear Surface Temperature (°C)	
	Experiment	UPM-FEM	Experiment	UPM-FEM
3003 aluminum (Al) alloy	3.3	3.7	501.2	616.8
Q235B steel	3	2.41	330.5	338.8

Fig. 1(b)). A total of 14,016 triangle elements were used. In the two NLTE regions, a fixed element size of 0.35 mm was used. In the plasma domain, the minimum element size near the center of the electric arc is 0.003 mm and the maximum element size far away from the center of the arc is 0.8 mm. In the anode domain, the minimum element size near the arc attached region is 8e-4 mm and the maximum element size away from the arc attached region is 0.4 mm. Furthermore, in the cathode region, the minimum element size is 0.012 mm near the cathode boundary and the maximum element size is 2.68 mm. Note that a mesh convergence study was carried out before the actual simulation studies to ensure that the solutions are not mesh-dependent.

Solver settings and computing time – The COMSOL time-dependent solver was used to execute the aforementioned UPM-FEM with an initial time increment of 1e-13 s and an automatic time stepping method. The average computing time on a 4-core 16 GB Ram laptop is about 30 min. A flow chart showing the calculation process is provided in Fig. 2.

2.3. Model validation against simulated lightning experiment test data

The effectiveness of the developed UPM-FEM has been verified in the second author's prior work [45] for a free-burning benchmark problem. In this study, the UPM-FEM is employed to study the lightning strike electric arc interaction with metallic materials. Before employing the UPM-FEM for analyzing the effects of amplitude-duration combinations, the model is validated by comparing with experimental test data [3,33,44] for a lightning continuing current with an amplitude of 404 A and a duration of 520 ms. The equivalent charge transfer is 210 C and the action integral is 8.4×10^4 A^2 s. The target materials (*i.e.,* anode material) are 3003 Aluminum (Al) alloy and Q235B steel, respectively, which are both common materials used in oil tanks and aircraft. The temperature distributions within the cathode-plasma-anode domain predicted by the UPM-FEM are shown in Fig. 3(a) for the Al alloy anode.

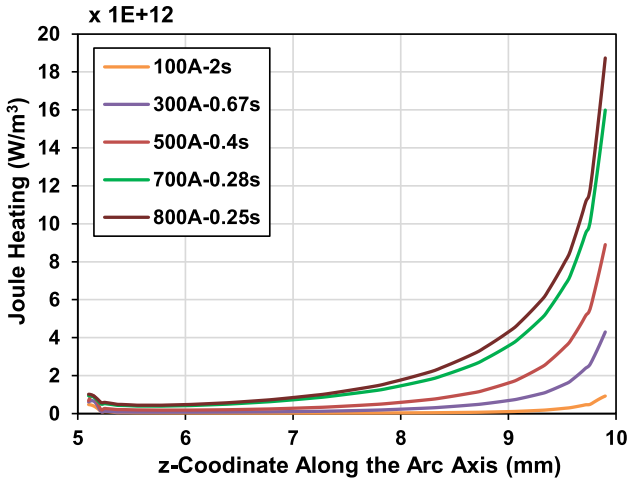

Fig. 4. Joule heating along the arc axis between cathode ($r = 0$, $z = 10$ mm, see the coordinate system in Fig. 3) and anode ($r = 0$, $z = 5$ mm) at different current amplitude-duration combinations.

The greatest penetration depth of the melting temperature (*i.e.,* 933 K for 3003 Al alloy) is taken as the criteria in evaluating the damage depth. The maximum temperature reaches approximately 29,800 K near the cathode tip in the plasma. Furthermore, the plasma flow reaches a maximum velocity of 248 m/s (see Fig. 3(b)).

As shown in Table 2, the predictions of the damage depth and the maximum rare-face temperature are 3.7 mm and 616.8 °C, respectively. The predictions are 12% larger for the damage depth and 18% higher for the temperature rise in comparison to the experimental data. For a Q235B steel sample, the predictions of the damage depth and the maximum rare-face temperature are 2.41 mm and 338.8 °C, respectively, which are 19% smaller and 2% higher than the experimental data. The difference between the model predictions and the experimental test data could be resulted from the uncertainties in the temperature-dependent material properties. Here, it is worth mentioning that the current UPM-FEM does not account for mechanical forces, such as the Marangoni force and arc drag force, which may also have contributed to the difference between model predictions and test data. Taking the additional mechanical constraints into the UPM-FEM will be a subject of our future work.

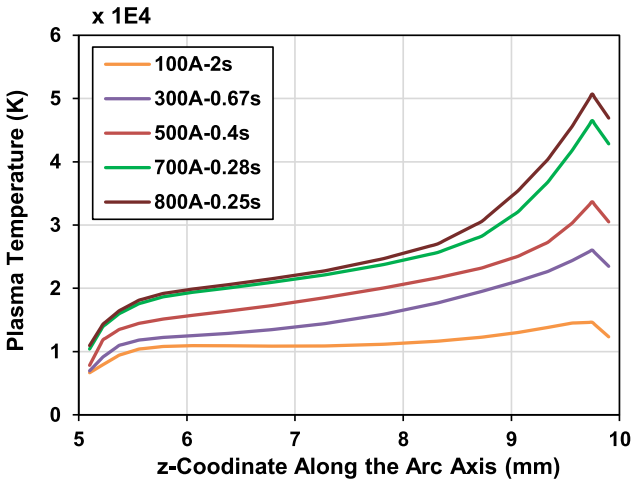

Fig. 5. Plasma temperature along the arc axis between cathode ($r = 0$, $z = 10$ mm) and anode ($r = 0$, $z = 5$ mm) at different current amplitude-duration combinations.

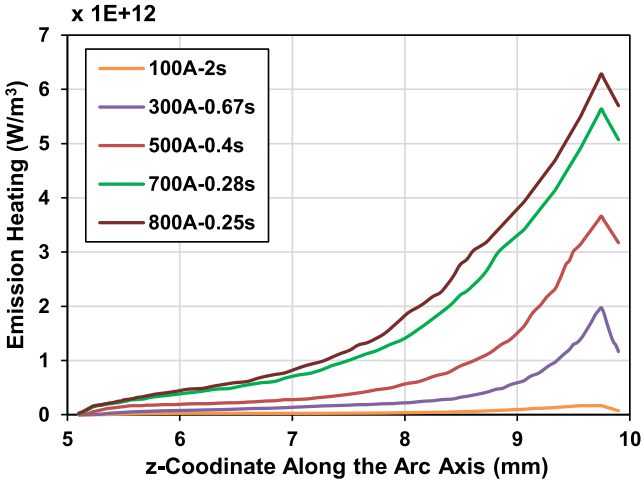

Fig. 6. Emission heat loss along the arc axis between cathode ($r = 0$, $z = 10$ mm) and anode ($r = 0$, $z = 5$ mm) at different current amplitude-duration combinations.

3. Influence of current amplitude-duration combinations on plasma energy

For the cathode-plasma-anode configuration, the competing mechanisms of the heating process of the plasma include the Joule heating, thermal conduction, radiative emission, and electronic enthalpic flux (*i.e.,* the energy contribution of the electrons due to the increase of their kinetic energy in the plasma column).

3.1. Effect of current amplitude-duration combinations on Joule heating

The Joule heating is determined by the current density and the electrical conductivity of plasma gas (J^2/σ). As shown in Fig. 4, after increasing the current amplitude from 100 A to 800 A for the simulated long continuous current, the Joule heating gets enhanced by 20 times to 1.8×10^{13} W/m^3. It is worth noting that a turning point shows up near the cathode ($z = 9.7$ mm), after which the Joule heating decreases more slowly for regions to the anode surface ($5 < z < 9.7$ mm). This is because the arc temperature peaks at $z = 9.7$ mm (see Fig. 5), which makes the plasma segment most conductive. Meanwhile, the plasma flow moves

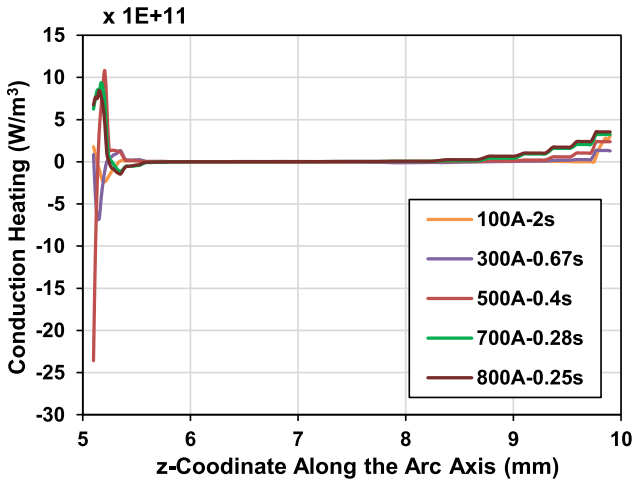

Fig. 7. Thermal conduction heating along the arc axis between cathode ($r = 0$, $z = 10$ mm) and anode ($r = 0$, $z = 5$ mm) at different current amplitude-duration combinations.

faster near the cathode (see Fig. 3(b)) and potentially decreases the electron density. Furthermore, we compared our predicted plasma temperature with the temperature profile on the anode surface reported by Ref. [4] and the maximum temperature in an arc plasma (shown in Fig. 5) reported by Refs. [35,48]. The predicted temperature on the anode surface agrees well with (difference = 2.7%) the numerical inversion result in Ref. [4]. The maximum arc temperature also shows good agreement (difference <5%) with the results for $I < 400$ A. Unfortunately, Refs. [35,48] terminated their analyses at current 400 A and no data were reported in the higher (>400 A) current regimes.

3.2. Effect of current amplitude-duration combinations on the radiative emission

The radiative power emission is dependent on the content of electrons in the ionized plasma and the net radiative emission coefficient. A stronger current source can ionize more particles and provide more electrons participating in the collision process, making this radiative emission item account for more energy loss. As shown in Fig. 6, the emission loss is strong at the region close to the cathode and attenuates significantly from the cathode to the anode. The peak emission loss occurs at the turning point ($z = 9.7$ mm, 0.3 mm away from the cathode surface), consistent with the turning point found in the profile of Joule heating in Fig. 4 and the plasma temperature in Fig. 5. This is because the plasma temperature increases from the cathode (due to electrons accelerating in the effect of the strong electric field from cathode) and peaks at the turning point, and then decreases along the plasma column to the anode. Meanwhile, the net emission coefficient has a nonlinear dependence on the plasma temperature and makes the variation curve of emission loss slightly deviate from the temperature variation. When the current amplitude rises from 100 A to 800 A, the peak emission loss at the turning point gets enhanced by 4.5 times and the increase of emission loss becomes modest at high current levels, which agrees with the saturation trend in the plasma temperature in Fig. 5.

3.3. Effect of current amplitude-duration combinations on the thermal conduction

Our simulation results show that different current amplitude-duration combinations represent different thermal conduction behaviors. As shown in Fig. 7, the sign of the conduction heating near the anode surface ($z = 5$ mm) changes from negative to positive when the electric current jumps from 300 to 700 A. The case of 500 A is right in

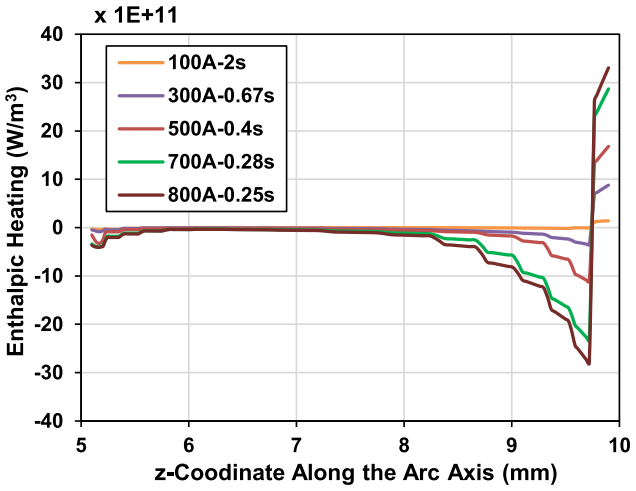

Fig. 8. Electronic enthalpic flux along the arc axis between cathode ($r = 0$, $z = 10$ mm) and anode ($r = 0$, $z = 5$ mm) at different current amplitude-duration combinations.

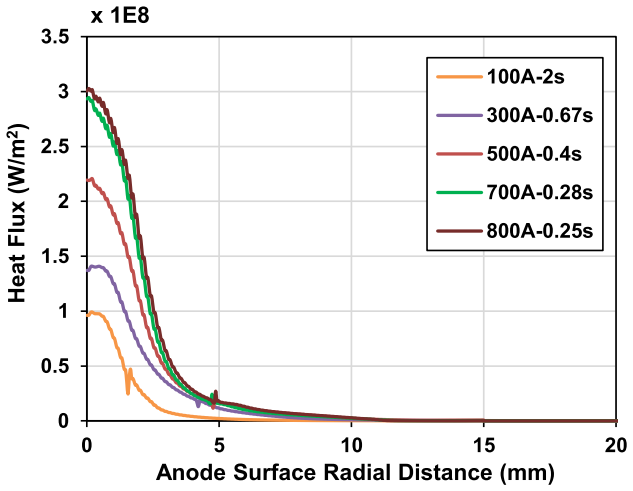

Fig. 9. Influence of the current amplitude-duration combinations on the heat flux along radial distance on the anode surface.

the middle of this transition and therefore an abrupt jump from a large negative value to a large positive value can be found near the anode surface. This nonlinear behavior of the thermal conduction is dictated by the strong nonlinear behavior of the thermal conductivity of the electric arc plasma as well as the rate of the temperature gradient change (*i.e.,* the second derivative of the temperature).

The thermal conduction heating in the middle region of the plasma between the anode and the cathode (from $z = 5.7$ to $z = 8$ mm) is relatively small when compared to the regions near the anode and the cathode surfaces. At the region near the cathode surface ($z \geq 8$ mm), the thermal conduction heating starts to slowly rise back. Also, as the current level increases, the thermal conduction heating near the cathode surface increases. For the case of 100 A, the thermal conduction heating at $z \geq 9.7$ mm shows a rapid increase, which differs from the rest of the cases where the thermal conduction heating starts to plateau above 9.7 mm. This difference is mainly attributed to the sudden drop of the plasma temperature at $z = 9.7$ mm (see Fig. 5), where the case of 100 A shows a slight drop, whereas the rest of the cases all show significant temperature drops. Furthermore, it can be noticed that the difference of the thermal conduction heating becomes smaller as the current level increases, which indicates a clear trend of saturation of the thermal conduction heating.

3.4. *Effect of current amplitude-duration combinations on the electronic enthalpic flux*

An increase in current amplitude can intensify the electric current density and raise the plasma temperature. As shown in Fig. 8, there is a sign change from positive to negative value at the turning point ($z = 9.7$ mm) for the electronic enthalpic flux. The sign of the enthalpic flux term is determined by the polarity of the current (negative in the model) and the temperature gradient. The temperature gradient shows a sign change at the turning point (see Fig. 5), which explains the positive-negative alteration. The enthalpic flux decreases along the plasma column from the cathode surface and down to the minimum at $z = 7.2$ mm, then rebounds moderately (to 4×10^{11} W/m^3 for $I = 800$ A) at $z = 5.8$ mm to the anode surface ($z = 5.1$ mm). This can be understood by the assumption of the LTE condition in the core plasma region and the disturbance by the NLTE state that is near the cathode or anode boundary. When the current amplitude increases, the enthalpic flux gets enhanced and can reach 2.8×10^{12} W/m^3 for $I = 800$ A.

3.5. *Summary*

From the above analysis, the four competing energy items, *i.e.,* the Joule heating, thermal conduction, radiative emission, and electronic enthalpic flux, generally increase with the rise of the current amplitude. At low current levels ($I < 300$ A), the four energy items are comparable in the order of magnitude and jointly determine the total energy injected to the test material. While with the current amplitude rising, the Joule heating, radiative emission, and electronic enthalpic flux increase significantly and lead to changes in the total energy of plasma in unit time. The contribution of the thermal conduction becomes less significant when compared to the overall plasma energy. A saturation trend can be found in the increase of these energy items at high current levels due to the convoluted physical processes and the non-monotonic functions of material parameters dependent on temperature.

4. Discussions on heat flux and damage response

For metal materials struck by lightning, the intense heat injection transferred from the plasma flow supplies the predominant energy in damaging materials' surface (*e.g.,* surface melting or evaporating). Therefore, the distributions of the heat flux on the material surface are most crucial in determining the damage depth.

4.1. *Effect of current amplitude-duration combinations on the heat flux*

As shown in Fig. 9, the peak heat flux at the arc center is 3×10^8 W/m^2 for the case of 800 A, *i.e,* a three-fold increase compared to the peak heat flux of 0.96×10^8 W/m^2 for the case of 100 A. A saturation trend for the increase of the peak heat flux with the rising current amplitude can be observed, which can be explained by the similar trend in the energy items of the Joule heating, radiative emission, and electronic enthalpic flux mentioned in Section 3.

On the anode surface, the heat flux attenuates remarkably along the radial distance away from the arc center. Meanwhile, the attenuation rate at higher current levels exhibits a steeper increase, or in other words, the heat flux decreases more sharply along the radial distance. This may be understood by two main aspects of changes: the first is that the emission loss becomes stronger and energy loss is more pronounced in bigger current conditions, while second is that the changes in the transport properties of plasma (*e.g.,* the thermal conductivity) have led to more heat conduction from the arc center region to its ambient margins.

Besides, the heat flux distribution on the anode surface is related to

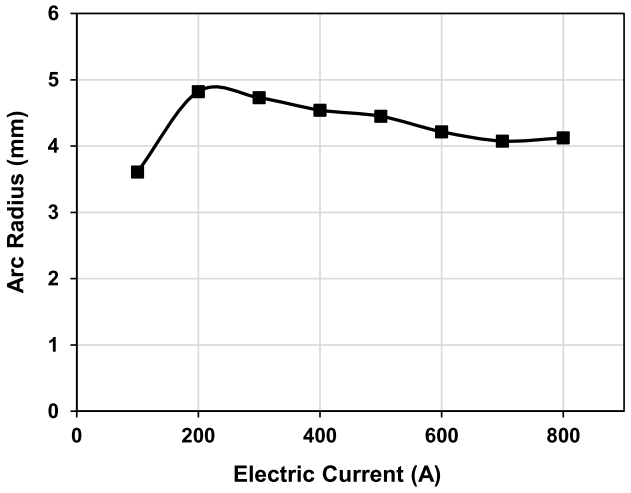

Fig. 10. Arc radius vs. electric current at a fixed charge transfer of 200 C.

the arc radius in the arc discharge. The modeling analysis provides the current density profiles, and hence, the arc radius changes in response to different current levels. We took the radius corresponding to 90% of the total arc current on the anode surface as the arc radius. The same criterion has also been adopted in Ref. [37]. The associated change of the arc radius as a function of the current level is shown in Fig. 10, where it can be seen that the arc radius increases as the current increases from 100 to 200 A, but decreases almost linearly as the current continues to increase to 700 A and finally plateaus at 800 A.

4.2. Effect of current amplitude-duration combinations on the damage depth

Fig. 11 illustrates the predicted damage response of 3003 Al alloy subjected to the different combinations. The damage depth and area get larger with the increasing charge transfer, consistent with the finding of the determinative role of charge transfer on the damage depth in Ref. [33]. Fig. 12 shows the increase of the damage depth as a function of the current level corresponding to three different charge transfer levels, *i.e.,* 120, 160, and 200 C (and hence different durations) predicted from our model and the experimental data at 167.4, 185.1, and 210.1 C [3,33,44]. Although some of the physics (*i.e.,* pressure loading and thermal strain effects) are not taken into account in the UPM-FEM, our predictions of the damage depth are still fairly consistent with the experimental test data. Note that these additional effects are quite insignificant compared to the melting of the metallic material. Our simulation results show that a higher constant current generally gives a higher arc pressure. The predicted peak arc pressure for the case with 800 A is 1.7 kPa, which agrees well with the result reported by Ref. [49] for a metal-inert-gas electric arc. With such low arc pressure, the resulting impact on mechanical deformation is expected to be insignificant. Moreover, a recent experimental study reported in Ref. [50] suggests that the effect of the lightning shockwave pressure is very insignificant compared to the effect of electric-thermal damage. Additionally, the thermal strain in the metallic materials caused by the lightning continuing current is in the order of 10^{-3} m/m, which is small compared to the threshold strain of the typical nonlinear deformation and failure for metallic materials (in the order of 10^{-2} m/m).

It can be noticed that for a fixed level of charge transfer, an increase in the current amplitude can lead to a greater damage depth. The increase in the damage results also shows a saturation trend at higher current amplitude (≥500 A), as shown in Figs. 11 and 12. This can be understood by the changes and similar saturation trend of the aforementioned heat flux. Therefore, it is evident that a current with a high amplitude (≥500 A) is more desirable for the simulated lightning strike continuing current tests in order to keep the consistency of the heat flux and current density flowing from the arc to the material surface, and hence, the corresponding material damage.

5. Conclusions

This work focused on analyzing the competing energy items of the lightning electric arc plasma, current density, heat flux, and the resulting damage of the material under different combinations of current amplitude-duration at a fixed charge transfer. Using a UPM-FEM, we found that at low current levels (≤300 A), the Joule heating, thermal conduction, radiative emission, and electronic enthalpic flux jointly determine the total energy injected to the test material. The increase of the electric current results in a continuous increase of the plasma temperature and the total energy. However, at higher current levels (≥500 A), the heat loss due to the radiative emission becomes more

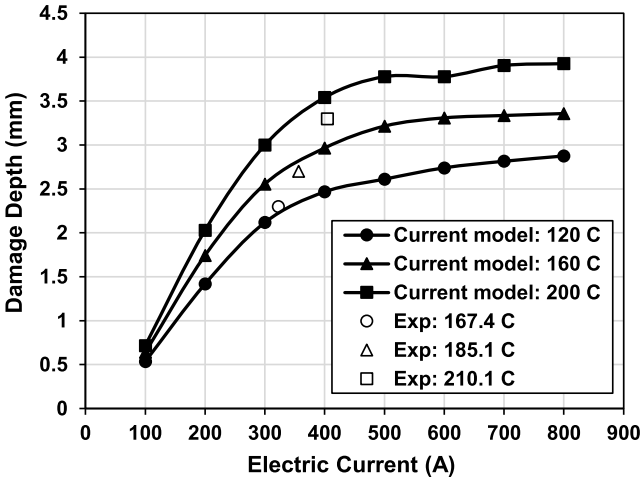

Fig. 12. The damage depth of the aluminum target material *vs.* the electric current used in the lightning strike continuing current test at different charge transfer levels and comparisons with experimental data.

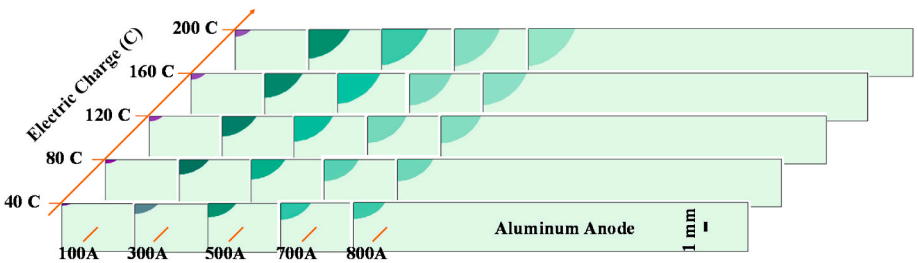

Fig. 11. Influence of the current amplitude-duration combinations on the damage depth of 3003 Al alloy resulted from the lightning continuing current at a fixed charge transfer.

pronounced. Meanwhile, the contribution of thermal conduction becomes less significant. Thus, as the current amplitude increases, the radiative emission heat loss quickly catches up with the heat gain due to the Joule heating, thermal conduction, and electronic enthalpic flux, leading to a saturation trend in the overall energy budget to damage materials.

For a fixed charge transfer of 200 C (±20%) in the lightning continuing current testing, the damage depth increases linearly as the electric current rises, when the current is less than 300 A. However, when the current gets above 500 A, the increase of the damage depth quickly slows down and plateaus. Therefore, to enable a testing environment that produces electric arc discharges with consistent electric arc properties and the material damage depth, it is recommended to choose a testing current with a higher amplitude (500–800 A) in the damage testing under the lightning continuing current component. Note that a severer and consistent material damage depth produced from simulated lightning strike tests allows to provide more conservative design guidance in the lightning strike protection of industrial objects.

Declaration of competing interest

The authors declare that they have no known competing financial interests or personal relationships that could have appeared to influence the work reported in this paper.

Data availability

Data will be made available on request.

Acknowledgments

Y. Liu would like to thank E. Williams and C. Zhang at MIT for many helpful discussions. In addition, Y. Liu would like to acknowledge the assistance of J. Chen and M. Dai at Shanghai Jiao Tong University for the implementation of the simulated lightning experiments and the financial support by National Natural Science Foundation of China (51907124) and National Key Research and Development Program of China (2017YFC1501506).

References

[1] J. Montañá Puig, F. Fabró Tàpia, O.A. Van der Velde, V. March Nomen, E. R. Williams, N. Pineda Ruegg, D. Romero Durán, Solà de las Fuentes G., Freijo Álvarez M., Global distribution of winter lightning: a threat to wind turbines and aircraft, Nat. Hazards Earth Syst. Sci. 16 (2016) 1465–1472.
[2] D. Wu, Z. Chen, Quantitative risk assessment of fire accidents of large-scale oil tanks triggered by lightning, Eng. Fail. Anal. 63 (2016) 172–181.
[3] Y. Liu, M. Dai, A. Guha, X. Gao, Z. Fu, Damage characteristics and microstructure response of steel alloy Q235B subjected to simulated lightning currents, IEEE Access 7 (2019) 9258–9264.
[4] Y. Liu, Z. Fu, Q. Liu, B. Liu, H. Xia, Numerical inversion analysis on front-face temperature rise of Al alloy suffered from long continuing current in lightning, IET Science, Meas. Technol. 12 (2018) 467–471.
[5] F. Moupfouma, Aircraft structure paint thickness and lightning swept stroke damages, SAE Int. J. Aerospace 6 (2013) 392–398.
[6] R. Brocke, F. Noack, F. Reichert, J. Schoenau, W. Zischank, The numerical simulation of the effects of lightning current arcs at the attachment point, in: 2001 International Conference on Lightning and Static Electricity (ICOLSE), SAE International, Seattle, Washington, Sep., 2001.
[7] G. Abdelal, A. Murphy, Nonlinear numerical modelling of lightning strike effect on composite panels with temperature dependent material properties, Compos. Struct. 109 (2014) 268–278.
[8] L. Chemartin, P. Lalande, B. Peyrou, A. Chazottes, P.Q. Elias, C. Delalondre, B. G. Cheron, F. Lago, Direct effects of lightning on aircraft structure: analysis of the thermal, electrical and mechanical constraints, AerospaceLab, 2012. AL05-09.
[9] Q. Dong, G. Wan, Y. Guo, L. Zhang, X. Wei, X. Yi, Y. Jia, Damage analysis of carbon fiber composites exposed to combined lightning current components D and C, Compos. Sci. Technol. 179 (2019) 1–9.
[10] P. Feraboli, M. Miller, Damage resistance and tolerance of carbon/epoxy composite coupons subjected to simulated lightning strike, Compos. Appl. Sci. Manuf. 40 (2009) 954–967.
[11] A.C. Garolera, S.F. Madsen, M. Nissim, J.D. Myers, J. Holboell, Lightning damage to wind turbine blades from wind farms in the US, IEEE Trans. Power Deliv. 31 (2014) 1043–1049.
[12] Y. Hirano, S. Katsumata, Y. Iwahori, A. Todoroki, Artificial lightning testing on graphite/epoxy composite laminate, Compos. Appl. Sci. Manuf. 41 (2010) 1461–1470.
[13] A. Katunin, K. Krukiewicz, R. Turczyn, P. Sul, A. Łasica, M. Bilewicz, Synthesis and characterization of the electrically conductive polymeric composite for lightning strike protection of aircraft structures, Compos. Struct. 159 (2017) 773–783.
[14] V. Kumar, T. Yokozeki, C. Karch, A.A. Hassen, C.J. Hershey, S. Kim, J.M. Lindahl, A. Barnes, Y.K. Bandari, V. Kunc, Factors affecting direct lightning strike damage to fiber reinforced composites: a review, Compos. B Eng. 183 (2020) 107688.
[15] J. Lee, P. Gharghabi, D. Boushab, T.M. Ricks, T.E. Lacy Jr., C.U. Pittman Jr., M. S. Mazzola, A. Velicki, Artificial lightning strike tests on PRSEUS panels, Compos. B Eng. 154 (2018) 467–477.
[16] P. Naghipour, E.J. Pineda, S.M. Arnold, Simulation of lightning-induced delamination in un-protected CFRP laminates, Appl. Compos. Mater. 23 (2016) 523–535.
[17] W. Lin, Y. Wang, Y. Aider, M. Rostaghi-Chalaki, K. Yousefpour, J. Kluss, D. Wallace, Y. Liu, W. Hu, Analysis of damage modes of glass fiber composites subjected to simulated lightning strike impulse voltage puncture and direct high voltage AC puncture, J. Compos. Mater. (2020), 0021998320927736.
[18] C. Karch, C. Paul, F. Heidler, Lightning strike protection of radomes, in: 2019 International Symposium on Electromagnetic Compatibility - EMC EUROPE, IEEE, Barcelona, Spain, 2019, pp. 650–655.
[19] F.S. Wang, Y. Zhang, X.T. Ma, Z. Wei, J.F. Gao, Lightning ablation suppression of aircraft carbon/epoxy composite laminates by metal mesh, J. Mater. Sci. Technol. 35 (2019) 2693–2704.
[20] Y. Wang, O.I. Zhupanska, Modeling of thermal response and ablation in laminated glass fiber reinforced polymer matrix composites due to lightning strike, Appl. Math. Model. 53 (2018) 118–131.
[21] Y. Wang, O.I. Zhupanska, Estimation of the electric fields and dielectric breakdown in non-conductive wind turbine blades subjected to a lightning stepped leader, Wind Energy 20 (2017) 927–942.
[22] Y. Wang, Modeling of Lightning-Induced Thermal Ablation Damage in Anisotropic Composite Materials and its Application to Wind Turbine Blades, PhD Dissertation, University of Iowa, 2016.
[23] W. Hu, W. Zhao, Y. Wang, Z. Liu, J. Cheng, J. Tan, Design optimization of composite wind turbine blades considering tortuous lightning strike and non-proportional multi-axial fatigue damage, Eng. Optim. 52 (2020) 1868–1886.
[24] S. Arinaga, K. Inoue, T. Matsushita, Experimental study for wind turbine blades lightning protection, in: Renewable Energy International Conference, Makuhari Messe, Chiba, Japan, 2006.
[25] Y. Wang, W. Hu, Investigation of the effects of receptors on the lightning strike protection of wind turbine blades, IEEE Trans. Electromagn C. 59 (2017) 1180–1187.
[26] V.A. Rakov, M.A. Uman, Lightning: Physics and Effects, Cambridge University Press, Cambridge, UK, 2003.
[27] SAE-ARP-5412, Aircraft Lightning Environment and Related Test Waveforms, 2005.
[28] MIL-STD-464, Electromagnetic Environmental Effects Requirements for Systems, US Department of Defense, 1997.
[29] Y. Wang, Multiphysics analysis of lightning strike damage in laminated carbon/glass fiber reinforced polymer matrix composite materials: a review of problem formulation and computational modeling, Compos. Appl. Sci. Manuf. 101 (2017) 543–553.
[30] V.A. Rakov, A review of triggered-lightning experiments, in: 30th International Conference on Lightning Protection, 2010.
[31] E. Rupke, Lightning Direct Effects Handbook, Lightning Technologies, in, Inc, Pittsfield, MA, USA, 2002.
[32] K. Yousefpour, W. Lin, Y. Wang, C. Park, Discharge and ground electrode design considerations for the lightning strike damage tolerance assessment of CFRP matrix composite laminates, Compos. B Eng. 198 (2020) 108226.
[33] L.I.U. Yakun, F.U. Zhengcai, L.I.U. Quanzhen, L.I.U. Baoquan, G. Anirban, Experimental and analytical investigation on metal damage suffered from simulated lightning currents, Plasma Sci. Technol. 19 (2017) 125301.
[34] International Eletrotechnical C, IEC 60060-1 Standard, High Voltage Test Techniques, 1994.
[35] J.J. Lowke, R. Morrow, J. Haidar, A simplified unified theory of arcs and their electrodes, J. Phys. Appl. Phys. 30 (1997) 2033.
[36] S.L.J. Millen, A. Murphy, G. Abdelal, G. Catalanotti, Sequential finite element modelling of lightning arc plasma and composite specimen thermal-electric damage, Comput. Struct. 222 (2019) 48–62.
[37] M. Tanaka, J.J. Lowke, Predictions of weld pool profiles using plasma physics, J. Phys. Appl. Phys. 40 (2006) R1.
[38] A. Traidia, F. Roger, E. Guyot, Optimal parameters for pulsed gas tungsten arc welding in partially and fully penetrated weld pools, Int. J. Therm. Sci. 49 (2010) 1197–1208.
[39] J.P. Trelles, Electrode patterns in arc discharge simulations: effect of anode cooling, Plasma Sources Sci. Technol. 23 (2014), 054002.
[40] L. Michael, S.T. Millmore, N. Nikiforakis, A multi-physics methodology for four states of matter, Commun. Appl. Math. Comput. (2019) 1–28.
[41] L. Chemartin, P. Lalande, C. Delalondre, B. Cheron, F. Lago, Modelling and simulation of unsteady dc electric arcs and their interactions with electrodes, J. Phys. Appl. Phys. 44 (2011) 194003.

[42] G.F. Abdelal, A. Murphy, A multiphysics simulation approach for efficient modeling of lightning strike tests on aircraft structures, IEEE Trans. Plasma Sci. 45 (2017) 725–735.
[43] F. Lago, J.J. Gonzalez, P. Freton, A. Gleizes, A numerical modelling of an electric arc and its interaction with the anode: Part I. The two-dimensional model, J. Phys. Appl. Phys. 37 (2004) 883.
[44] Y. Liu, H. Xia, Z. Fu, X. Gao, B. Liu, Analysis on the choosing of test electrode for lightning current metal ablation experiments, in: 33rd International Conference on Lightning Protection, IEEE, Estoril, Portugal, Sep., 2016, pp. 1–6.
[45] Y. Aider, Y. Wang, G.F. Abdelal, O.I. Zhupanska, Modeling of the electric arc plasma discharge produced by a lightning strike continuing current, in: 2019 International Conference on Lightning and Static Electricity (ICOLSE), Wichita, Kansas, USA, Sep., 2019.
[46] M.I. Boulos, P. Fauchais, E. Pfender, Thermal Plasmas: Fundamentals and Applications, Springer Science & Business Media, 2013.
[47] M. Capitelli, G. Colonna, C. Gorse, A. d'Angola, Transport properties of high temperature air in local thermodynamic equilibrium, Eur. Phys. J. D-Atomic Mol. Plasma Phys. 11 (2000) 279–289.
[48] J. Haidar, A.J.D. Farmer, Surface temperature measurements for tungsten-based cathodes of high-current free-burning arcs, J. Phys. Appl. Phys. 28 (1995) 2089.
[49] A.B. Murphy, M. Tanaka, K. Yamamoto, S. Tashiro, J.J. Lowke, K. Ostrikov, Modelling of arc welding: the importance of including the arc plasma in the computational domain, Vacuum 85 (2010) 579–584.
[50] Y. Hirano, T.N.T. Sonehara, An experimental study on influence of shockwave on composite lightning damage, in: 2019 International Conference on Lightning and Static Electricity (ICOLSE), Wichita, Kansas, USA, Sep., 2019.